SCIENTIFIC REPORTS
natureresearch

OPEN

# Control of the Thermoelectric Properties of $Mg_2Sn$ Single Crystals via Point-Defect Engineering

Wataru Saito[1], Kei Hayashi[1*], Jinfeng Dong[2], Jing-Feng Li[2] & Yuzuru Miyazaki[1]

**$Mg_2Sn$ is a potential thermoelectric (TE) material that can directly convert waste heat into electricity. In this study, $Mg_2Sn$ single-crystal ingots are prepared by melting under an Ar atmosphere. The prepared ingots contain Mg vacancies ($V_{Mg}$) as point defects, which results in the formation of two regions: an $Mg_2Sn$ single-crystal region without $V_{Mg}$ (denoted as the single-crystal region) and a region containing $V_{Mg}$ (denoted as the $V_{Mg}$ region). The $V_{Mg}$ region is embedded in the matrix of the single-crystal region. The interface between the $V_{Mg}$ region and the single-crystal region is semi-coherent, which does not prevent electron carrier conduction but does increase phonon scattering. Furthermore, electron carrier concentration depends on the fraction of $V_{Mg}$, reflecting the acceptor characteristics of $V_{Mg}$. The maximum figure of merit $zT_{max}$ of $1.4(1) \times 10^{-2}$ is realised for the $Mg_2Sn$ single-crystal ingot by introducing $V_{Mg}$. These results demonstrate that the TE properties of $Mg_2Sn$ can be optimised via point-defect engineering.**

Thermoelectric (TE) materials, which are capable of converting waste heat into electricity, are expected to play a significant role in future energy utilisation and management[1,2]. The performance of TE materials is evaluated in terms of the dimensionless figure of merit, $zT = S^2\sigma T/\kappa$, and power factor $PF = S^2\sigma$, where $S$, $\sigma$, $T$ and $\kappa$ are the Seebeck coefficient, electrical conductivity, absolute temperature and thermal conductivity, respectively. Recently, point defects (interstitials, vacancies and antisite defects) in TE materials have been recognised as an important factor that significantly affects the TE performance in the following two ways. First, the carrier concentration in a TE material can be optimised by tuning the fraction of point defects because they can act as acceptors or donors, which results in an increase in PF. Second, thermal conductivity can be reduced by introducing point defects because they can act as phonon scattering centres. Although enhanced $zT$ values have been realised for a variety of TE materials via point-defect engineering[3–15], the fraction of point defects has rarely been evaluated quantitatively. Thus, point-defect engineering cannot yet be considered an established strategy to enhance TE performance.

Recently, our group performed the crystal structure analysis of polycrystalline $Mg_2Si$ samples and quantitatively verified the presence of interstitial defects in the samples using single-crystal X-ray diffraction (SC-XRD)[16,17]. In the present study, we focus on $Mg_2Sn$ with the same crystal structure as $Mg_2Si$. $Mg_2Sn$ has been studied extensively as a potential TE material[18–37]. Xin *et al.*[31] reported that an Sb-doped n-type polycrystalline $Mg_2Sn$, $Mg_{2.15}Sn_{0.98}Sb_{0.02}$ exhibited a $zT$ value of 0.53 at 650 K ($\kappa$ and PF are 4.7 W/mK and 3.9 W/mK$^2$, respectively). Chen *et al.*[22] reported that an Ag-doped p-type polycrystalline $Mg_2Sn$, $Mg_2Sn$ + 0.5 at. % Ag exhibited a $zT$ value of 0.30 at 450 K ($\kappa$ and PF are 4.0 W/mK and 2.6 W/mK$^2$, respectively). Despite these sufficiently high PF values, the $\kappa$ values are also high, limiting the $zT$ values lower than ~0.5. Although the importance of controlling point defects in $Mg_2Sn$ is highlighted in some literature[29,31], quantitative analysis of point defects has not been performed so far.

Regarding the TE properties of pristine $Mg_2Sn$, single crystals exhibited different $S$ values depending on the preparation method, as shown in Table 1[18–23]. Generally, different $S$ values reflect differences in carrier concentration. Liu *et al.*[32] predicted that possible point defects in $Mg_2Sn$ are Mg vacancies ($V_{Mg}$) at the 8*c* (1/4 1/4 1/4) site and Mg interstitial defects ($Mg_i$) at the 4*b* (1/2 1/2 1/2) site. These point defects are ionised and generate hole and electron carriers in $Mg_2Sn$, respectively, i.e. $V_{Mg} \rightarrow V_{Mg}^{2-} + 2h^+$ and $Mg_i \rightarrow Mg_i^{2+} + 2e^-$. Thus, it is suggested that the difference in $S$ values between $Mg_2Sn$ single crystals prepared using different methods arises from varying

[1]Department of Applied Physics, Graduate School of Engineering, Tohoku University, Sendai, 980-8579, Japan. [2]State Key Laboratory of New Ceramics and Fine Processing, School of Materials Science and Engineering, Tsinghua University, Beijing, 100084, China. *email: hayashik@crystal.apph.tohoku.ac.jp

| Preparation conditions | | | | | | | |
|---|---|---|---|---|---|---|---|
| Method | Composition | Melting temp. (K) | $P_{Ar}$ (atm) [c] | Crystalline | $S_{@300\,K}$ (μV/K) | $\sigma_{@300\,K}$ (S/cm) | Ref. |
| Melt growth | $Mg_2Sn$ | 1093 | 0.8 | PC[d] | −45 | 23 | 18 |
| | $Mg_{2.04}Sn$ | | | | −66 | 1350 | |
| | $Mg_{2.05}Sn$ | 1073 | 0.8 | | −53 | 22 | 19 |
| | $Mg_{2.06}Sn$ | | | | −39 | 34 | |
| | $Mg_{2+\delta}Sn$ | 1123 | $10^{-10}$ | | −23 | 25 | 20 |
| Bridgeman | $Mg_{2.1}Sn$ | 1093 | 0.8 | SC[e] | −52 | 26 | 21 |
| RF[a] | $Mg_{2.1}Sn$ | 1093 | 0.8 | PC[d] | 50 | 27 | 22 |
| HGDS[b] | $Mg_{2.34}Sn$ | 1200 | 0.03 | SC[e] | −261 (parallel to [111]) | 49 | 23 |
| | | | | | 159 (parallel to [1−10]) | 29 | |
| | | | | | 149 (parallel to [11−2]) | 30 | |

**Table 1.** Reported $S$ and $\sigma$ values for $Mg_2Sn$ measured at 300 K. [a]Radio Frequency (RF). [b]High-temperature Gradient Directional Solidification (HGDS). [c]Ar pressure ($P_{Ar}$). [d]Polycrystal (PC). [e]Single-crystal (SC).

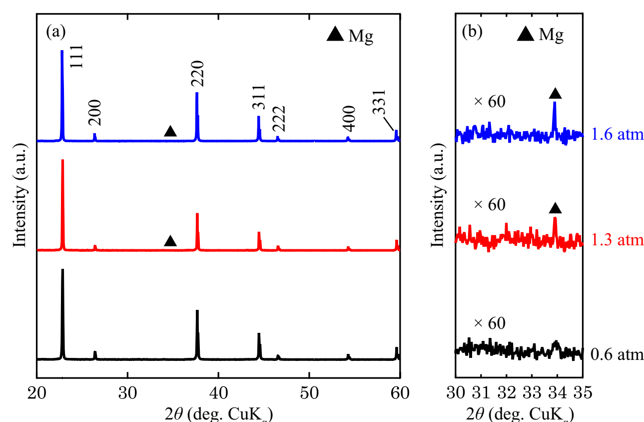


**Figure 1.** (**a**) Powder X-ray diffraction patterns of the prepared $Mg_2Sn$ ingots and (**b**) an enlargement of the regions between 30° and 35°.

fractions of $V_{Mg}$ and/or $Mg_i$. Li *et al.*[23] reported that $Mg_2Sn$ single crystals exhibited anisotropic $S$ values. However, it is possible that the fractions of $V_{Mg}$ and/or $Mg_i$ in the single crystals used were different because each $Mg_2Sn$ single crystal along the [111], [1$\bar{1}$0], or [11$\bar{2}$] direction was prepared by cutting from different parts of one $Mg_2Sn$ single-crystal ingot.

To reveal the relationship between point defects and the TE properties of $Mg_2Sn$, we prepared $Mg_2Sn$ single-crystal ingots by melting under an Ar atmosphere. In the prepared ingots, $V_{Mg}$ exists as a point defect, the fraction of which was successfully evaluated by SC-XRD. Furthermore, the $V_{Mg}$ fraction is controlled by changing the Ar pressure, $P_{Ar}$. We find a peculiar nanostructure relating to $V_{Mg}$ via transmission electron microscope (TEM); the $Mg_2Sn$ single crystals with $V_{Mg}$ form nanometer-sized regions and are embedded in the $Mg_2Sn$ single-crystal region without $V_{Mg}$. The TE properties ($|S|$, $\sigma$ and $\kappa$) of the ingots all decrease with increasing $V_{Mg}$ because of a decrease in the electron carrier concentration and an enhancement of phonon scattering. In particular, the $\kappa$ value is extremely low compared with that of polycrystalline $Mg_2Sn$ reported in the literature[28], which is discussed in relation to the nanostructure of the ingots.

## Results and Discussion

### Phase characterisation and crystal structure refinement.

Figure 1 shows the powder XRD patterns of the $Mg_2Sn$ single-crystal ingots prepared under $P_{Ar} = 0.6$, 1.3 and 1.6 atm (hereafter, these ingots are referred to as the 0.6-, 1.3- and 1.6-atm ingots, respectively). All of the XRD peaks are well indexed to the expected $Mg_2Sn$ phase, except for a small peak assigned to an Mg secondary phase found for the 1.3- and 1.6-atm ingots. The bulk XRD measurements confirm the high crystallinity of the ingots. In the bulk XRD patterns, peaks corresponding to the 111, 222 and 333 planes are found (Fig. S1a). In addition, the full width at half maximum of the rocking curves of the 111 peak are as small as 317.3, 438.8 and 453.9 arcsec for the 0.6-, 1.3- and 1.6-atm ingots, respectively (Fig. S1b). A homogeneous distribution of the constituent elements is observed in the SEM-EDX mapping

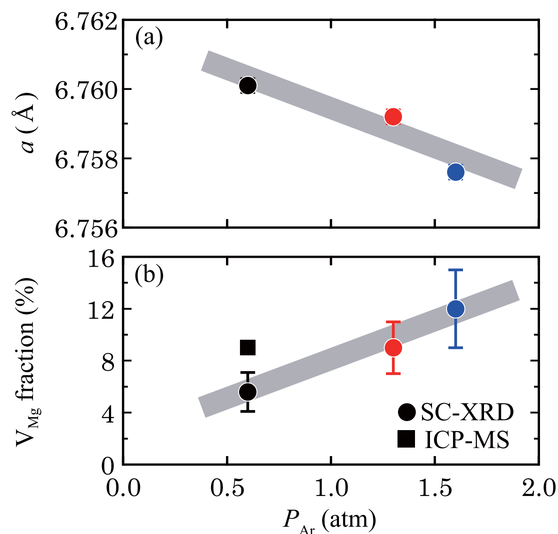


**Figure 2.** Dependence of the (**a**) lattice constant and (**b**) $V_{Mg}$ fraction evaluated by single-crystal X-ray diffraction (SC-XRD) and inductively coupled plasma mass spectrometry (ICP-MS) on Ar pressure, $P_{Ar}$.

images of the $Mg_2Sn(111)$ cleavage surface, as shown in Fig. S2, further verifying the high quality of the prepared ingots. The Mg secondary phase is not observed in the SEM-EDX images because of its insignificant amount.

Single-crystal structure refinement was performed to evaluate the fraction of point defects (a detailed description can be found in the Supporting Information). As shown in Fig. 2a, the lattice constant decreases from 6.7625(2) Å to 6.7576(2) Å with increasing $P_{Ar}$, suggesting a change in chemical composition and/or mutual substitution between Mg and Sn. In other words, the fraction of point defects changes. In fact, the $Mg_2Sn$ single-crystal ingots contain $V_{Mg}$, the fraction of which increases from 5.6(15)% to 12(3)% with increasing $P_{Ar}$ (Fig. 2b). The presence of $V_{Mg}$ is confirmed by the inductively coupled plasma mass spectrometry (ICP-MS) measurement for the 0.6-atm ingot. These results indicate that the $V_{Mg}$ fraction is controllable by changing $P_{Ar}$. The increase in $V_{Mg}$ induced by increasing $P_{Ar}$ can be attributed to the decreased formation energy of $V_{Mg}$, as reported for the case of Si that formation energy for a Si vacancy is calculated to decrease with increasing hydrostatic pressure[38].

**Nanostructure characterisation.** The nanostructure of the 0.6-atm ingot was observed using TEM. Figure 3a shows a low-magnification TEM image, in which white and grey regions are observed. The grey regions are dispersed in the white region spread throughout the ingot. As shown in Fig. 3b, a high-magnification TEM image of the white region exhibits a perfect atomic arrangement of the $Mg_2Sn(111)$ surface, indicating that the white region corresponds to the $Mg_2Sn$ single-crystal region without $V_{Mg}$ (denoted as the single-crystal region). This is confirmed by the fast Fourier transform (FFT) image of the white region, which shows the diffraction pattern of $Mg_2Sn$ along the [111] orientation (inset of Fig. 3b).

On the other hand, a high-magnification TEM image of the grey region exhibits a parallel Moiré pattern (Fig. 3c). Generally, a parallel Moiré pattern is observed when the electron beam of the TEM passes through two stacked crystals that have slightly different lattice constants[3,39–43]. Figure S4 shows a simple illustration of this situation. In the present study, the introduction of $V_{Mg}$ into $Mg_2Sn$ reduces the lattice constant, as mentioned above (see Fig. 2a). Thus, it is conceivable that the observed parallel Moiré pattern originates from the stacking of the $Mg_2Sn$ single crystal with $V_{Mg}$ on the single-crystal region. In other words, the $Mg_2Sn$ single crystals with $V_{Mg}$ form nanometer-sized regions (denoted as $V_{Mg}$ regions) that are distributed in the matrix of the single-crystal region. This means that $V_{Mg}$ tends to aggregate in the ingot, which is considered to be energetically stable because the formation energy of point defects is generally lowered by clustering. The size distribution of the $V_{Mg}$ regions was analysed, and it is plotted in Fig. 3d. The average size and density of the $V_{Mg}$ region are 11 nm and $2.4(1) \times 10^{14}\,m^{-2}$, respectively.

To further investigate the interface between the $V_{Mg}$ region and the single-crystal region, an FFT image was produced from the area enclosed in the red dashed square in Fig. 4a, which covers both regions in the 0.6-atm ingot, as shown in the inset of Fig. 4a. The diffraction pattern of the single-crystal region (indicated by the white circles) and some extra spots (indicated by the red circles) are observed. Figure 4b shows the inverse FFT (IFFT) image generated from the diffraction pattern of the single-crystal region, which reproduces the regular atomic arrangement of the $Mg_2Sn(111)$ surface and is identical to that shown in Fig. 3b. In the IFFT image transformed from the extra spots, some aligned interference fringes are observed around the interface (the red solid line in Fig. 4c). As shown in the filtered IFFT image (Fig. 4d,e) obtained from the two spots in the inset of Fig. 4a (indicated by the red arrows), dislocations (red symbols) can be seen near the interference fringes. From the TEM observation of the 0.6-atm ingot, the dislocation density was evaluated to be $3.5 \times 10^{16}\,m^{-2}$ in the ingot, indicating that the interface between the $V_{Mg}$ region and the single-crystal region is semi-coherent. Such semi-coherent interfaces are often formed when the lattice mismatch between a precipitate and a matrix is sufficiently small[3,39–43].

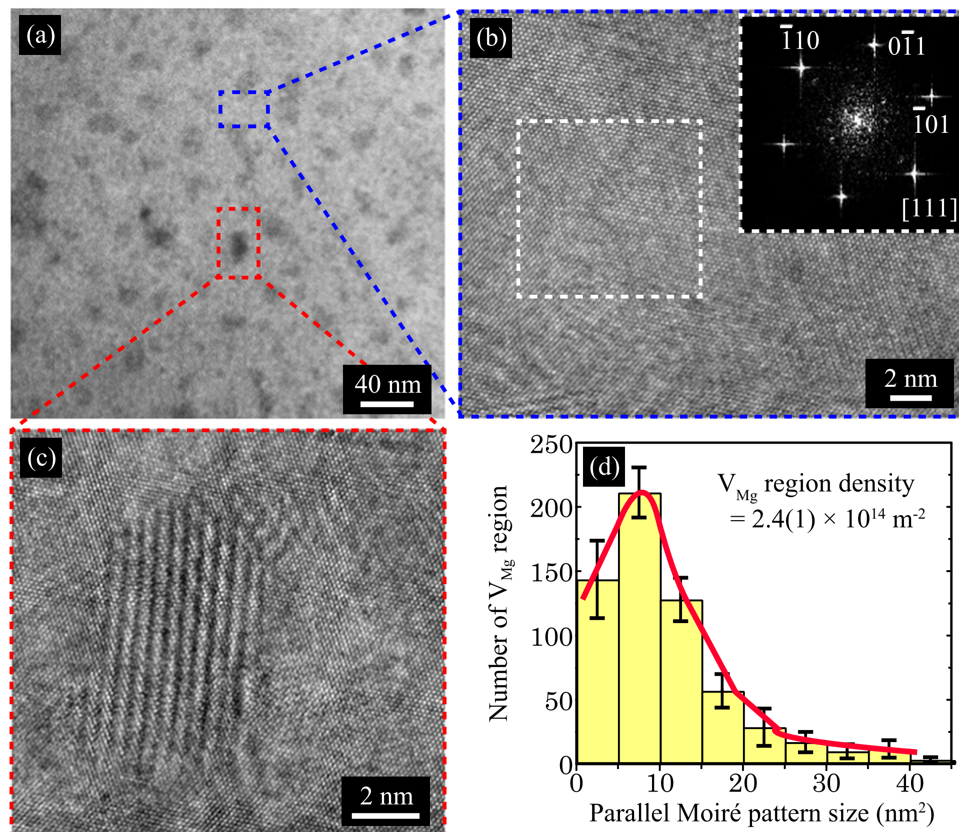


**Figure 3.** (**a**) Low-magnification transmission electron microscopy (TEM) image of the 0.6-atm ingot. (**b**) High-magnification TEM image of the blue dashed square region in (**a**). The inset shows a fast Fourier transform (FFT) image of the white dashed square region. (**c**) High-magnification TEM image of the red dashed square region in (**a**), in which a parallel Moiré pattern is observed. (**d**) Size distribution of the parallel Moiré pattern corresponding to the location of the $Mg_2Sn$ single crystal with Mg vacancies (namely, the $V_{Mg}$ region).

The difference in the lattice constants between the $Mg_2Sn$ single crystals with and without $V_{Mg}$ (corresponding to the $V_{Mg}$ region and the single-crystal region) is smaller than 0.01 Å, as can be seen in Fig. 2a, which can be an origin of the formation of the semi-coherent interface.

**Thermoelectric properties measurements.** In addition to changing the carrier concentration, the introduction of $V_{Mg}$ may cause carrier and phonon scattering through the formation of nanosized $V_{Mg}$ regions and semi-coherent interfaces. To reveal the relationship between the $V_{Mg}$ fraction and the electrical properties of the $Mg_2Sn$, the Seebeck coefficient, $S$, and the electrical conductivity, $\sigma$, of the 0.6-, 1.3- and 1.6-atm ingots were measured. The temperature dependence of $S$ is shown in Fig. 5a. All ingots exhibit negative $S$, i.e. the majority carriers are electrons, which is also confirmed by the negative Hall coefficient of the ingots measured at 300 K. The $|S|$ value at 300 K decreases from $|-166|$ μV/K to $|-115|$ μV/K as $P_{Ar}$ increases, indicating that the electron carrier concentration is different for each ingot. Upon the increase of the temperature, the differences between the $|S|$ values diminish and become negligible above 450 K. These tendencies are attributed to the enhanced bipolar diffusion because $Mg_2Sn$ is narrow band gap semiconductor[21,23,44,45]. Figure 5b shows the temperature dependence of $\sigma$. The ingots exhibit similar $\sigma$ values over the entire measurement temperature range. The $\sigma$ value at 300 K slightly decreases from 32 S/cm to 26 S/cm as $P_{Ar}$ increases.

The $S$ and $\sigma$ values at 300 K are plotted against the $V_{Mg}$ fraction in the insets of Fig. 5a,b, respectively. To determine the reason for the decrease in both $|S|$ and $\sigma$ with increasing $V_{Mg}$ fraction, the electron carrier concentration, $n$, at 300 K was evaluated from Hall effect measurements. Figure 5c shows that $n$ decreases from $2.23(3) \times 10^{18}$ cm$^{-3}$ to $1.25(1) \times 10^{18}$ cm$^{-3}$ with increasing $V_{Mg}$ fraction, indicating that $V_{Mg}$ acts as an acceptor and cancels a part of the electron carriers in $Mg_2Sn$. The change rate of per percentage unit of $V_{Mg}$ is $1 \times 10^{17}$ cm$^{-3}$%$^{-1}$. Generally, $|S|$ should increase with decreasing $n$; however, $|S|$ decreases in the present study. The controversial behaviour can be explained by assuming that the Fermi level is located near the middle of the band gap. This assumption is reasonable because the ingots are considered intrinsic semiconductors, which is supported by the tendency of $\sigma$ and $|S|$ of the ingots to increase and decrease with increasing temperature, respectively, and the fact that the $\sigma$ values at 300 K are as low as several tens of S/cm. In this case, the $|S|$ value decreases as the Fermi level moves toward the middle of the band gap upon increasing the $V_{Mg}$ fraction, which is what we observed for the $Mg_2Sn$ single-crystal ingots in the present study. Turning to the relation between $\sigma$ and $n$, the rate at which $\sigma$ decreases is lower than that for $n$. This means that the carrier mobility, $\mu$, increases

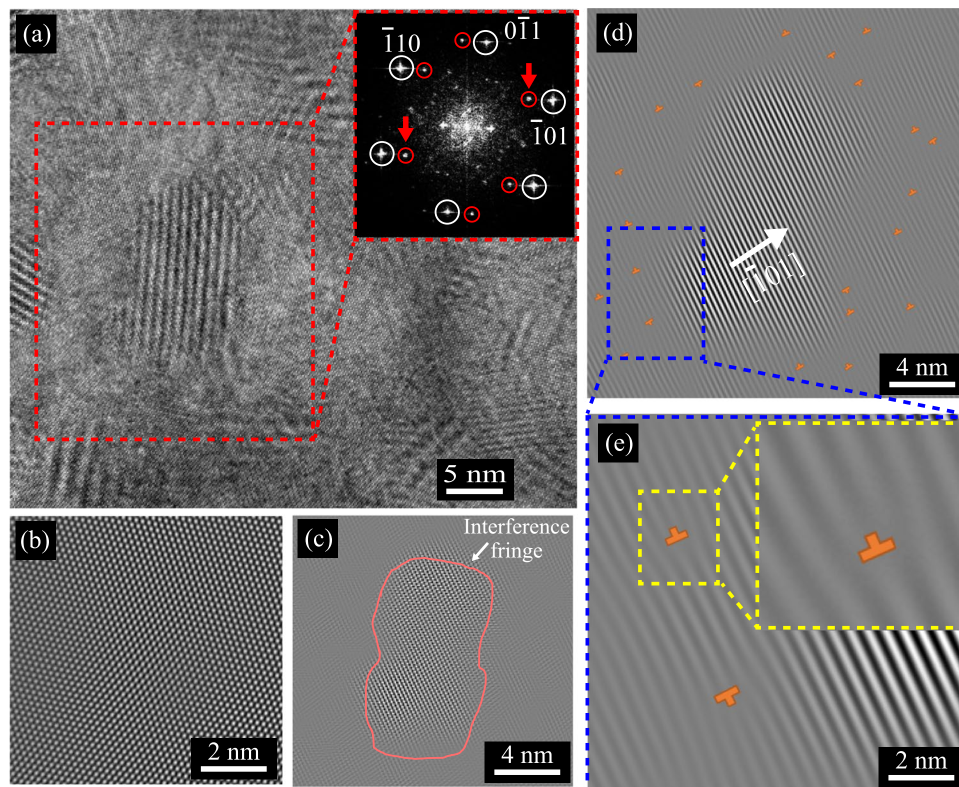


**Figure 4.** (**a**) High-magnification TEM image of the 0.6-atm ingot. The inset shows a FFT image of the red dashed square region, including the $Mg_2Sn$ single-crystal regions with and without $V_{Mg}$. Using the diffraction spots marked with the white circles and red circles in the inset, inverse FFT (IFFT) images were generated, as shown in (**b**,**c**), respectively. (**d**) IFFT image transformed from the two spots indicated by red arrows in the inset of (**a**). (**e**) Magnified image of the blue dashed region in (**d**). Dislocations are marked in orange in (**d**,**e**).

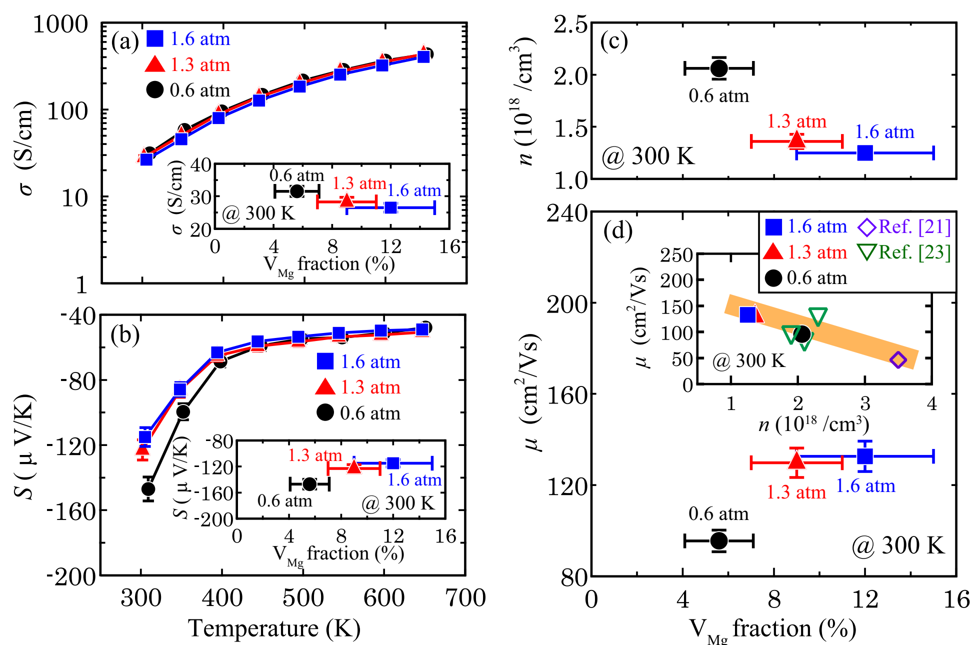


**Figure 5.** Temperature dependence of (**a**) $\sigma$ and (**b**) $S$ of the prepared ingots. These insets show the relation between $\sigma$ and $S$ at 300 K and $V_{Mg}$ amount, respectively. Dependence of (**c**) $n$ and (**d**) $\mu$ on the $V_{Mg}$ amount. The inset of (**d**) plots $n$ vs. $\mu$.

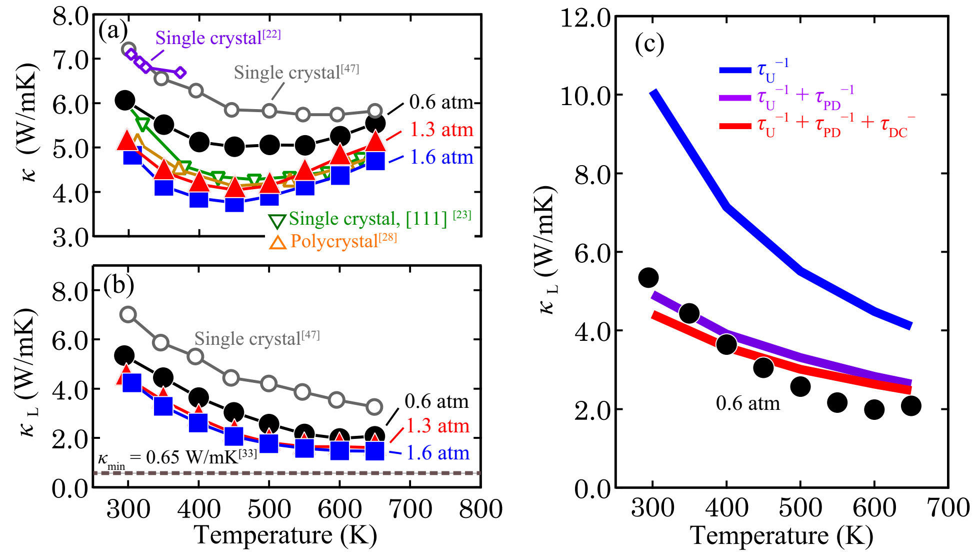


**Figure 6.** Temperature dependence of (**a**) $\kappa$ and (**b**) $\kappa_L$ of the 0.6-atm ingot. (**c**) Comparison of $\kappa_L$ with the theoretical calculation. In the calculation, phonon scattering due to the Umklapp process ($\tau_U^{-1}$), point defects ($\tau_{PD}^{-1}$) and dislocation cores ($\tau_{DC}^{-1}$) was considered.

with increasing $V_{Mg}$ fraction. As shown in Fig. 5d, $\mu$ increases from 89.9(8) $cm^3$/Vs to 132.6(28) $cm^3$/Vs, which is inversely proportional to $n$. Such a relation between $n$ and $\mu$ has also been reported for an $Mg_2Si$ single crystal[46]. The $\mu$ values of the $Mg_2Sn$ single-crystal ingots as a function of $n$ is shown in the inset in Fig. 5d, which are on an extrapolated line from the reported data of $Mg_2Sn$ single-crystal ingots[21,23], implying that $V_{Mg}$ does not act as a carrier scattering centre. From these results, it is concluded that the introduction of $V_{Mg}$ actually changes $n$ in the $Mg_2Sn$ single-crystal ingots, but does not affect $\mu$, probably owing to the semi-coherent interface between the $V_{Mg}$ region and the single-crystal region. We should recall that the $Mg_2Sn$ single-crystal ingots prepared in this study are not uniform in morphology; the $V_{Mg}$ regions are dispersed in the single-crystal region. Thus, the $\sigma$, $S$, $n$ and $\mu$ values described above are macroscopic physical properties over the whole ingot, i.e., they are actually weighed means considering the contributions from the $V_{Mg}$ regions and the single-crystal region. The changes in the $\sigma$, $S$, $n$ and $\mu$ values with increasing $V_{Mg}$ fraction originate from the different $\sigma$, $S$, $n$ and $\mu$ values between the $V_{Mg}$ regions and the single-crystal region. In other words, the $V_{Mg}$ regions have lower $\sigma$, $S$ and $n$ values and higher $\mu$ value than the single-crystal region.

Next, the thermal conductivity, $\kappa$, of the 0.6-, 1.3- and 1.6-atm ingots was measured (Fig. 6a). As $P_{Ar}$ increases, i.e. the $V_{Mg}$ fraction increases, $\kappa$ significantly decreases. The 1.6-atm ingot exhibits lower $\kappa$ than the $Mg_2Sn$ single crystals and polycrystals reported in previous literatures[21,23,25,30]. The minimum $\kappa$ of 3.75(2) W/mK is realised for the 1.6 atm ingot at 450 K. By subtracting the carrier thermal conductivity, $\kappa_e$ (Fig. S5a), and the bipolar thermal conductivity, $\kappa_{bp}$ (Fig. S5b), from $\kappa$, the lattice thermal conductivity, $\kappa_L$, was estimated as shown in Fig. 6b. (For the estimation of $\kappa_e$, we used the Wiedemann-Frantz law. The deviation of the estimation and the details of the $\kappa_e$ and $\kappa_{bp}$ calculations are given in the Supporting Information.) Upon the increase of $P_{Ar}$, the $\kappa_L$ value of the ingots approaches the minimum calculated $\kappa_L$ reported in the literature[31]. The lowest $\kappa_L$ of 1.47(1) W/mK is recorded for the 1.6-atm ingot at 650 K, which is still lower than the literature values[21,23,28,47].

To elucidate the reason for this low $\kappa_L$, $\kappa_L$ was calculated using the Debye model[48].

$$\kappa_L = \left(\frac{k_B}{2\pi^2 v}\right)\left(\frac{k_B T}{\hbar}\right)\int_0^{\frac{\theta_D}{T}}\left(\frac{x^4 e^x}{\tau_{tot}^{-1}(e^x - 1)^2}dx, \qquad x \equiv \frac{\hbar\omega}{k_B T}, \right. \tag{1}$$

where $\hbar$, $\omega$, $k_B$, $v$, $\theta_D$ and $\tau_{tot}$ are the reduced Plank constant, phonon frequency, Boltzmann constant, average sound velocity, Debye temperature and total relaxation time for phonon scattering, respectively. Considering the presence of $V_{Mg}$ and semi-coherent interfaces in the ingot, phonon scattering by point defects and dislocation cores, in addition to the Umklapp process, was included in the calculation. Under these assumptions, $\tau_{tot}$ is given by $\tau_{tot}^{-1} = \tau_U^{-1} + \tau_{PD}^{-1} + \tau_{DC}^{-1}$, where $\tau_U$, $\tau_{PD}$ and $\tau_{DC}$ are the relaxation times corresponding to the Umklapp process, point defects and dislocation cores, respectively. More details of the equations expressing these relaxation times and the relevant parameters, such as the average atomic mass, can be found in Tables S4 and S5. As can be seen in Fig. 6c, the calculated result matches well with the experimental $\kappa_L$ of the 0.6-atm ingot. It is found that point defects originating from $V_{Mg}$ significantly contribute to the lower $\kappa_L$ of the ingot. By contrast, the dislocations at the interface between the $V_{Mg}$ region and the single-crystal region have a smaller effect on $\kappa_L$ compared with the point defects probably because the concentration of dislocations ($3.5 \times 10^{16}\,m^{-2}$) is lower than the concentration of point defects ($1.3(3) \times 10^{18}\,m^{-2}$). Therefore, it is concluded that $V_{Mg}$ has the main effect of lowering $\kappa_L$ of the $Mg_2Sn$ single-crystal ingots, but the semi-coherent interface does not lead to as much phonon scattering as $V_{Mg}$.

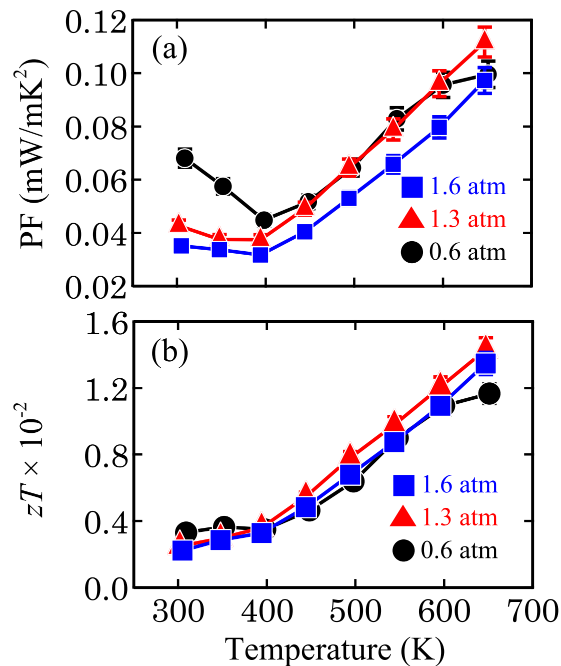


**Figure 7.** Temperature dependence of (**a**) power factor, PF, and (**b**) dimensionless figure of merit, $zT$, of the prepared ingots.

Finally, the PF and $zT$ values of the 0.6-, 1.3- and 1.6-atm ingots were calculated, and the results are plotted in Fig. 7a,b, respectively. At temperatures below 450 K, the PF value decreases with increasing $P_{Ar}$, reflecting the variation in $|S|$ among the ingots. Above 450 K, the prepared ingots show similar PF values because the difference in $S$ and $\sigma$ between the ingots is small, but slightly higher PF values are obtained for the 0.6- and 1.3-atm ingots relative to the 1.6-atm ingot. The highest PF is 0.11(1) mW/mK$^2$ at 650 K for the 1.3-atm sample. Regarding $zT$, the 0.6- and 1.3-atm ingots show higher $zT$ values than the other ingots in the temperature ranges from 300 to 400 K and from 400 to 650 K, respectively. The maximum $zT$ value is $1.4(1) \times 10^{-2}$ at 650 K for the 1.3-atm ingot mainly because of its low $\kappa$. In this study, we have succeeded in evaluating the $V_{Mg}$ fraction in $Mg_2Sn$ single-crystal ingots. The TE properties are optimised by controlling the $V_{Mg}$ fraction, demonstrating that point-defect engineering is an effective strategy to enhance the PF and $zT$ of $Mg_2Sn$. The superiority of the $Mg_2Sn$ single-crystal ingots with $V_{Mg}$ prepared in this study is low $\kappa$, but PF and $zT$ are still low. (The comparison of $\kappa_{min}$, $PF_{max}$ and $zT_{max}$ of the 0.6-, 1.3- and 1.6-atm with those of other $Mg_2Sn$ single crystals reported in the literatures[21,23] is shown in Fig. S6.) By combining the reduction of $\kappa_L$ (<1.5 W/mK) via point defect engineering, as in this study, with the enhancement of PF (~4.0 mW/mK$^2$) via a conventional doping method[31], a higher $zT$ value ($zT > 0.9$ at 650 K) can be achieved for a $Mg_2Sn$ single crystal.

## Methods

$Mg_2Sn$ single-crystal ingots were synthesised by melting using a one-zone-controlled resistive-heating furnace. Mg grains (4 N, Mitsuwa Chemicals Co., Ltd, 4 × 4 mm) and Sn powder (4 N, Kojundo Chemical Lab., 63 μm pass) were weighed and charged into a boron-nitride-coated alumina crucible in a molar ratio of Mg:Sn = 2.2:1. The crucible was then enclosed in a quartz tube under an Ar atmosphere of pressure, $P_{Ar}$ = 0, 0.6, 1.3, or 1.6 atm at room temperature. The tube was heated to 1093 K over 9 h, then cooled to 973 K slowly over 48 h and finally cooled to room temperature over 9 h.

The crystalline phases and crystallinity of the $Mg_2Sn$ single-crystal ingots were investigated by powder and bulk X-ray diffraction (XRD) using Cu Kα radiation (D8 ADVANCE, Bruker AXS). For the bulk XRD measurements, the $Mg_2Sn$(111) cleavage surface was used. Moreover, a rocking curve of the 111 peak was measured. Owing to the difficulty in crystal structure refinement using the powder XRD patterns of $Mg_2Sn$, as was the case for $Mg_2Si$[16,17], the fraction of point defects was evaluated via single-crystal XRD (SC-XRD) using Mo Kα radiation (D8 VENTURE, Bruker AXS). Small $Mg_2Sn$ single-crystal particles with typical dimensions of 40 μm × 60 μm × 60 μm, selected from fractured $Mg_2Sn$ single-crystal ingots, were used for the SC-XRD measurements. Single-crystal structure refinement was performed using the JANA2006 crystallographic computing system[49]. The fraction of point defects was also examined by inductively coupled plasma–mass spectrometry (ICP-MS, Agilent 8800 ICP-QQQ, Agilent Technologies). The morphology and nanostructure of the $Mg_2Sn$ single-crystal ingots were observed using a scanning electron microscope equipped with an energy-dispersive X-ray spectrometer (SEM-EDX; JSM-IT100, JEOL) and a field-emission-type TEM (JEM-2100F, JEOL).

The Seebeck coefficient, $S$, and the electrical conductivity, $\sigma$, of the $Mg_2Sn$ single-crystal ingots were measured in vacuum using an automated thermoelectric tester (RZ2001i, Ozawa Science Co.). The Hall coefficient, $R_H$, was

measured using a physical properties measurement system (PPMS, Quantum Design) at 300 K by sweeping the magnetic field from −5.0 T to 5.0 T. The carrier concentration, $n$, and carrier mobility, $\mu$, were calculated using the equations $n = |1/(eR_H)|$ and $\mu = \sigma R_H$, respectively, where $e$ is the elementary charge. The thermal conductivity, $\kappa$, was measured in vacuum using a standard laser flash analyser (TC-7000, ULVAC-RIKO).

Received: 16 December 2019; Accepted: 23 January 2020;
Published online: 06 February 2020

## References

1. Goldsmid, H. J. *Applications of thermoelectricity*; Methuen Monograph: London (1960).
2. Rowe, D. M. *Thermoelectrics Handbook Macro to Nano*; CRC Press: Boca Raton (2006).
3. Kim, S. I. *et al*. Dense Dislocation Arrays Embedded in Grain Boundaries for High-performance Bulk Thermoelectrics. *Sci* **348**, 109–114 (2015).
4. Li, J. *et al*. Low-Symmetry Rhombohedral GeTe Thermoelectrics. *Joule* **2**, 976–987 (2018).
5. Day, T. *et al*. Influence of Compensating Defect Formation on the Doping Efficiency and Thermoelectric Properties of $Cu_{2-y}Se_{1-x}Br_x$. *Chem. Mater.* **27**, 7018–7027 (2015).
6. Jiang, G. *et al*. High Performance $Mg_2$ (Si,Sn) Solid Solutions: a Point Defect Chemistry Approach to Enhancing Thermoelectric Properties. *Adv. Funct. Mater.* **24**, 3776–3781 (2014).
7. Zhu, T. *et al*. New Insights into Intrinsic Point Defects in $V_2VI_3$ Thermoelectric Materials. *Adv. Sci.* **3**, 160004 (2016).
8. Xin, J. *et al*. Mg Vacancy and Dislocation Strains as Strong Phonon Scatterers in $Mg_2Si_{1-x}Sb_x$ Thermoelectric Materials. *Nano Energy* **34**, 428–436 (2017).
9. Hu, L. *et al*. Point Defect Engineering of High-Performance Bismuth-Telluride-Based Thermoelectric Materials. *Adv. Funct. Mater.* **24**, 5211–5218 (2014).
10. Li, Z. *et al*. Defect Chemistry for Thermoelectric Materials. *J. Am. Chem. Soc.* **138**, 14810–14819 (2016).
11. Chen, Z. *et al*. Lattice Dislocations Enhancing Thermoelectric PbTe in Addition to Band Convergence. *Adv. Mater.* **29**, 1606768 (2017).
12. Bhat, D. K. & Shenoy, S. U. High Thermoelectric Performance of Co-Doped Tin Telluride Due to Synergistic Effect of Magnesium and Indium. *J. Phys. Chem. C* **121**, 7123–7130 (2017).
13. Shenoy, S. U. & Bhat, D. K. Enhanced Bulk Thermoelectric Performance of $Pb_{0.6}Sn_{0.4}$ Te: Effect of Magnesium Doping. *J. Phys. Chem. C* **121**, 20696–20703 (2017).
14. Shenoy, S. U. & Bhat, D. K. Bi and Zn Co-doped SnTe Thermoelectrics: Interplay of Resonance Levels and Heavy Hole Band Dominance Leading to Enhanced Performance and a Record High Room Temperature ZT. *J. Mater. Chem. C*, https://doi.org/10.1039/C9TC06490G (2020).
15. Bhat, D. K. & Shenoy, S. U. Enhanced Thermoelectric Performance of Bulk Tin Telluride: Synergistic Effect of Calcium and Indium Co-doping. *Mater. Today Phys.* **4**, 12–18 (2018).
16. Kubouchi, M. *et al*. Quantitative Analysis of Interstitial Mg in $Mg_2Si$ Studied by Single Crystal X-ray Diffraction. *J. Alloys Compd.* **617**, 389–392 (2014).
17. Kubouchi, M. *et al*. Effect of Interstitial Mg in $Mg_{2+x}Si$ on Electrical Conductivity and Seebeck Coefficient. *J. Electron. Mater.* **45**, 1589–1593 (2015).
18. Chen, H. Y. & Savvides, N. Microstructure and Thermoelectric Properties of n- and p-Type Doped $Mg_2Sn$ Compounds Prepared by the Modified Bridgman Method. *J. Electron. Mater.* **38**, 1056–1060 (2009).
19. Chen, H. Y. & Savvides, N. Eutectic Microstructure and Thermoelectric Properties of $Mg_2Sn$. *J. Electron. Mater.* **39**, 1792–1797 (2010).
20. Kim, S. *et al*. Electronic Structure and Thermoelectric Properties of P-type Ag-doped $Mg_2Sn$ and $Mg_2Sn_{1-x}Si_x$ ($x = 0.05, 0.1$). *J. Appl. Phys.* **116**, 153706 (2014).
21. Chen, H. Y. & Savvides, N. Thermoelectric Properties and Microstructure of Large-Grain $Mg_2Sn$ Doped with Ag. *Mater. Res. Soc. Symp. Proc.* 1166 (2009).
22. Chen, H. Y. *et al*. Electronic and Thermal Transport Properties of $Mg_2Sn$ Crystals Containing Finely Dispersed Eutectic Structures. *Phys. Status Solidi A* **207**, 2523–2531 (2010).
23. Li, X. *et al*. Anisotropy of Seebeck Coefficient in un-doped $Mg_2Sn$ Single Crystal. *Intermetallics* **81**, 26–31 (2010).
24. Varma, R. R. *et al*. Effect of Magnesium and Silver Doping on the Thermoelectric Performance of Cast $Mg_2Sn$ Alloys. *J. Alloys Compd.* **757**, 142–149 (2018).
25. Winkler, U. Die elektrischen Eigenschaften der intermetallischen Verbindungen $Mg_2Si$, $Mg_2Ge$, $Mg_2Sn$ und $Mg_2Pb$. *Helv. Phys. Acta* **28**, 633–666 (1955).
26. Zaitsev, V. K. *et al*. Width of Forbidden Band in Solid Solutions $Mg_2Si$-$Mg_2Sn$. *Sov. Phys. Solid State* **11**, 3000–3002 (1969).
27. Aizawa, T. & Song, R. Mechanically Induced Reaction for Solid-state Synthesis of $Mg_2Si$ and $Mg_2Sn$. *Intermatellics* **14**, 382–391 (2006).
28. An, T. *et al*. Enhancement of p-type Thermoelectric Properties in an $Mg_2Sn$ System. *J. Korean Phys. Soc.* **60**, 1717–1723 (2012).
29. Mao, J. *et al*. Thermoelectric Performance Enhancement of $Mg_2Sn$ Based Solid Solutions by Band Convergence and Phonon Scattering via Pb and Si/Ge Substitution for Sn. *Phys. Chem. Chem. Phys.* **18**, 20726–20737 (2016).
30. Tani, J. *et al*. Thermoelectric Properties of Impurity-Doped $Mg_2Sn$. *J. Electron. Mater.* **48**, 3330–3335 (2019).
31. Xin, J. *et al*. Multiscale Defects as Strong Phonon Scatters to Enhance Thermoelectric Performance in $Mg_2Sn_{1-x}Sb_x$ Solid Solutions. *Small Methods* 1900412 (2019).
32. Liu, X. *et al*. Significant Roles of Intrinsic Point Defects in $Mg_2X$ ($X = $ Si, Ge, Sn) Thermoelectric. *Materials. Adv. Electron. Mater.* **2**, 1500284 (2016).
33. Jin, Y. *et al*. $Mg_2Sn$: a Potential Mid-temperature Thermoelectric Material. *RSC Adv.* **6**, 48728–48736 (2016).
34. Tani, J. & Kido, H. Impurity Doping into $Mg_2Sn$: A First-Principles Study. *Physica B* **407**, 3493–3498 (2012).
35. Pulikkotil, J. J. *et al*. Doping and Temperature Dependence of Thermoelectric Properties in $Mg_2$(Si,Sn). *Phys. Rev. B* **86**, 155204-1–8 (2012).
36. Safavi, M. *et al*. Thermoelectric Properties Improvement in $Mg_2Sn$ Thin Films by Structural Modification. *J. Alloys Compd.* **692**, 137601 (2019).
37. Tani, J. & Ishikawa, H. Thermoelectric Properties of $Mg_2Sn$ Thin Films Fabricated Using Radio Frequency Magnetron Sputtering. *Thin Solid Films* **404**, 4558–4560 (2019).
38. Gusakov, V. *et al*. Formation of Frenkel Pairs and Diffusion of Self-Interstitial in Si Under Normal and Hydrostatic Pressure: Quantumchemical Simulation. *Physica B* **404**, 4558–4560 (2009).
39. Murray, C. B. *et al*. Synthesis and Characterization of Nearly Monodisperse Cd $E$ ($E = $ Sulfur, Selenium, Tellurium) Semiconductor Nanocrystallites. *J. Am. Chem. Soc.* **115**, 8706–8715 (1993).
40. Chadderton, L. T. *et al*. Stacking Faults in Cadmium Sulphide. *Nature* **198**, 573–574 (1963).
41. Rhyee, J.-S. *et al*. Peierls Distortion as a Route to High Thermoelectric Performance in $In_4Se_{3-\delta}$ Crystals. *Nature* **459**, 965–968 (2009).

42. Perumal, S. *et al*. Low Thermal Conductivity and High Thermoelectric Performance in Sb and Bi Codoped GeTe: Complementary Effect of Band Convergence and Nanostructuring. *Chem. Mater.* **29**, 10426–10435 (2017).
43. Zhou, M. *et al*. Nanostructured $AgPb_mSbTe_{m+2}$ System Bulk Materials with Enhanced Thermoelectric Performance. *J. Am. Chem. Soc.* **130**, 4527–4532 (2008).
44. Shenoy, S. U. & Bhat, D. K. Electronic Structure Engineering of Tin Telluride Through Co-doping of Bismuth and Indium for High Performance Thermoelectrics: a Synergistic Effect Leading to a Record High Room Temperature ZT in Tin Telluride. *J. Mater. Chem. C* **7**, 4817–4821 (2019).
45. Bhat, D. K. & Shenoy, S. U. Zn: A Versatile Resonant Dopant for SnTe Thermoelectrics. *Mater. Today Phys*. 100158, https://doi.org/10.1016/j.mtphys.2019.100158 (2019).
46. Udono, H. *et al*. Crystal Growth and Characterization of $Mg_2Si$ for IR-Detectors and Thermoelectric Applications. *Jpn. J. Appl. Phys.* **54**, 07JB06 (2015).
47. Martin, J. J. Thermal Conductivity of $Mg_2Si$, Mg Ge and $Mg_2Sn$. *J. Phys. Chem. Solids* **33**, 1139–1148 (1972).
48. Callawey, J. & Vonbaeyer, H. C. Effect of Point Imperfections on Lattice Thermal Conductivity. *Phys. Rev.* **120**, 1149–1154 (1960).
49. Petricek, V. *et al*. Crystallographic Computing System JANA2006: General features. *Z. Kristallogr.* **229**, 345–352 (2014).

## Acknowledgements

The authors are grateful to Mr. K. Yoza from the single-crystal diffraction application at Bruker Japan for part of the single-crystal XRD measurements. The authors are grateful to Mr. T. Miyazaki and Mr. S. Takahashi from the Instrumental Analysis Group at Tohoku University for the TEM and inductively coupled plasma mass spectrometry measurements. W.S. and K.H. are also grateful to Prof. H. Udono from the Faculty of Engineering at Ibaraki University for his advice on fabricating high-quality $Mg_2Sn$ single-crystal ingots. This work was partly supported by the Grant-in-Aid for Scientific Research (B) (No. 17H03398) and Grant-in-Aid for Scientific Research on Innovative Areas (No. 17H05207) from the Ministry of Education, Culture, Sports, Science, and Technology of Japan, and by Tsinghua-Tohoku Collaborative Research Fund.

## Author contributions

W.S. performed the synthesis of ingots, XRD, SEM and thermoelectric measurements and wrote the initial draft of the manuscript. K.H. contributed to discussion of data and assisted in the preparation of the manuscript. J.D. and J.-F.L. contributed to discussions. Y.M. supervised the project and contributed to discussions and writing. All authors have approved the final version of the manuscript.

## Competing interests

The authors declare no competing interests.

## Additional information

**Supplementary information** is available for this paper at https://doi.org/10.1038/s41598-020-58998-1.

**Correspondence** and requests for materials should be addressed to K.H.

**Reprints and permissions information** is available at www.nature.com/reprints.

**Publisher's note** Springer Nature remains neutral with regard to jurisdictional claims in published maps and institutional affiliations.

**Open Access** This article is licensed under a Creative Commons Attribution 4.0 International License, which permits use, sharing, adaptation, distribution and reproduction in any medium or format, as long as you give appropriate credit to the original author(s) and the source, provide a link to the Creative Commons license, and indicate if changes were made. The images or other third party material in this article are included in the article's Creative Commons license, unless indicated otherwise in a credit line to the material. If material is not included in the article's Creative Commons license and your intended use is not permitted by statutory regulation or exceeds the permitted use, you will need to obtain permission directly from the copyright holder. To view a copy of this license, visit http://creativecommons.org/licenses/by/4.0/.

© The Author(s) 2020